Hindawi
Advances in Civil Engineering
Volume 2020, Article ID 7525692, 18 pages
https://doi.org/10.1155/2020/7525692

Research Article

Application Research of New Cementitious Composite Materials in Saline Soil Subgrade Aseismic Strengthening

Shuai Huang, Yuejun Lyu, and Yanju Peng

Institute of Crustal Dynamics, China Earthquake Administration, Beijing 100085, China

Correspondence should be addressed to Shuai Huang; huangshuai3395@163.com

Received 5 August 2019; Revised 31 October 2019; Accepted 13 November 2019; Published 3 January 2020

Guest Editor: Endong Wang

Saline soil affected by earthquakes and groundwater can lead to subgrade subsidence and collapse in highway construction. Consequently, considering the potential activity of the waste slag and magnesia, new cementitious composite materials used in solid saline soil were developed in our study. The unconfined compressive strengths of the saline soil solidified by the new cementitious composite materials with a combination of magnesium oxide, calcium oxide, gypsum, and mineral powder and cement were investigated, and the optimum dosage proportion of the new cementitious composite material for solidifying saline soil was determined; then the SEM, EDS, and XRD of the saline soil solidified by the new cementitious composite materials and cement were analysed. The research result showed that the saline soil solidified by our newly developed cementitious composite material showed compact internal structure and uniformly distributed soil particles; moreover, the new cementitious composite material exhibited a favourable solidifying effect on harmful ions in saline soil, and the Cl^- trapping capacity of the new cementitious composite materials was stronger than that of cement. Finally, our developed cementitious composite material was applied to saline soil subgrade strengthening, and the displacement, acceleration, excess pore water pressure, and damage degree of the subgrade strengthening by our newly developed cementitious composite materials decreased remarkably; therefore, our newly developed cementitious composite material can improve the seismic behaviour of the saline soil subgrade and show potential future engineering application value.

1. Introduction

As a special rock and soil mass, saline soil shows a high structural strength in its natural state due to cementation caused by the salt. The soil structure is easily damaged when the saline soil is immersed in water, which can lead soluble salt to be dissolved and greatly decrease the bearing capacity and compression modulus of the saline soil. Compared with nonsaline soil, saline soil is a special kind of soil in engineering practice because it comprises a significant amount of soluble salt; as a result, the engineering properties of saline soil are complicated. Saline soil is widely distributed in Northwest China, where the areal distribution of saline soil reaches about 60% of saline-alkali land area of China [1]. The western region of China is prone to destructive earthquakes. If saline soil is used as subgrade filling, subgrade soil will be subjected to plastic deformation under the repeated effect of earthquake-induced dynamic loads, thus leading to cracking and failure of pavement structures (Figure 1); therefore, the purpose of this study is to develop new cementitious composite materials to solidify saline soil in a subgrade and improve the seismic behaviour of the saline soil subgrade.

Saline soil subgrades are likely to collapse such as differential settlement and cracking affected by various factors including groundwater and seismic load. At present, the methods for solidifying saline soil involve dynamic compaction, soil replacement, lowering groundwater level, and application of solidifying materials [2, 3]. Wen et al. [4] determined the key technical parameters for soil layer grading of saline soil subgrades, which provided a technical reference for solidifying saline soil subgrades. Song et al. [5] used the soil replacement method to solidify the saline soil subgrades, and it had a favourable strengthening effect. Zhang et al. [6] studied the influence of overburden load on the salt expansion of the saline soil subgrade with different salt contents, water contents, and initial dry density

(a) (b)

Figure 1: Saline soil-induced pavement cracking and settlement.

conditions, and they found that the salt expansion rate of the saline soil decreased significantly with the increase of the overburden pressure. Zhang et al. [7] used various measures to reinforce the stability of a saline soil subgrade and found that saline soil solidification is an economical method. Li et al. [8] used gravel to solidify the saline soil subgrade and found that the gravel plays an important role in improvement of the gradation of the saline soil. Qingfeng et al. [9] used a nuclear magnetic resonance (NMR) technique to test the microstructural characteristics of the saline soil solidified with different proportions of water glass, lime and fly ash, lime, fly ash, and water glass, respectively, and analysed the solidifying effect of the saline soil. Research showed that saline soil stabilised by solidifying materials exhibited a higher strength [10–12]; however, solidifying materials also suffer certain disadvantages. For example, saline soil solidified by utilising lime has poor water stability; the strength of saline soil solidified with fly ash is low; saline soils solidified by using cement and high-performance cementitious composite materials are expensive. From the perspective of effectively utilising resources, saving resources, and protecting the environment, the application of slag in industrial cementitious materials is of interest in many countries around the world. Slag has potential activity which is latent unless activated under certain conditions, such as the mechanical activation method, chemical activation method, and high-temperature activation method. Based on practical engineering experience, the chemical activation method is used in our study.

Magnesia (MgO) is often used to activate the potential activity of the cementitious composite materials. The dosage of MgO in clinker of the Portland slag cement cannot exceed 5.0%, which is stipulated in Chinese standard [13]. If the cement satisfies that standard after being subjected to a test of cement soundness using the autoclave method, the content of MgO in clinker is allowed to reach 6.0% at most. Light-burned MgO shows a series of advantages including small grains, significant lattice distortion, a comparatively looser structure, and high activity. Therefore, many scholars are studying the use of light-burned MgO. Jin and Wang [14] developed a new inorganic cementitious composite material using blast furnace slag, light-burned MgO, alkali-water glass, and potassium hydroxide, and the material showed favourable mechanical properties. Lou et al. [15] developed double-expansive cement by adding MgO into low-heat microexpansive cement, and the cement also exhibited synchronous expansion by virtue of aluminite and MgO. Harrison [16] developed new cementitious materials by adding a certain amount of active MgO into Portland cement, together with about 80% fly ash. Liska et al. [17] developed new cementitious materials by blending active MgO, volcanic ash, and hydraulic cement, which realised shrinkage compensation through hydration of active MgO with magnesium hydroxide. Inspired by the above studies, new cementitious composite materials were developed using mineral powder, magnesia, quicklime, and gypsum in our study, and compression strength tests, water stability tests, measurement of the soluble ion contents, SEM (scanning electron microscope) analysis, EDS (energy dispersive spectrometer) energy spectrum analysis, and XRD (X-ray diffractometer) analysis of the saline soil solidified by the new cementitious composite materials were investigated. Finally, the new cementitious composite material was applied to strengthen a saline soil subgrade located in a highly seismic region, and our study provides important technological guidance for seismic design of a saline soil subgrade.

2. Test Analysis

2.1. Specimen Preparation. The new cementitious composite materials were prepared using slag, building gypsum, quicklime, and magnesia, and the chemical activation method is used in our study. The samples of saline soil solidified by the new cementitious composite materials were made according to the standard [18] of TB10113-96 *Technical Code on Dry Jet Mixing Method to Stabilise Soft Foundations*, and the specific steps are as follows:

(1) The air-dried saline soil was crushed and screened through a 5 mm square aperture sieve, and water was added into the specimen configured as natural moisture gravimetric content 29.7%

(2) The solidified soil was uniformly packed into cubic testing moulds; then, the moulds were vibrated for 3 min on a shaking table at 3000 ± 200 cycles/min, and the vibration amplitude is 0.35 ± 0.05 mm

(3) The prepared samples of solidified soil are shown in Figure 2, and the samples are cured in a moist air

cabinet at the temperature of $(20 \pm 3)^{\circ}$C and a relative humidity of 75%

By analysing main chemical compositions of the blast furnace slag, the chemical compositions contents are shown in Table 1.

The new cementitious composite material was made by using slag, building gypsum, quicklime, and magnesia, and the key properties of the mineral powders are listed in Table 2.

The Portland slag cement (P·S·B32.5R) used in this study was purchased from Tangshan Jidong Cement Co., Ltd, Hebei Province, China, and its main performance indices are listed in Table 3.

The saline soil from Northwest China was used, and its key components of soluble salt were analysed, as shown in Table 4.

It can be seen in Table 2, $Cl^-/SO_4 > 2$. Therefore, the saline soil was classified as a chlorine saline soil. When the average salinity in soil was in the range of 1 to 5, saline soil was subordinated to an intermediate saline soil. According to the above analysis of soluble salt contents, the average salinity of the test soil was 1.39; thus, the saline soil in our study was classified as intermediate saline soil.

2.2. Test Methods

2.2.1. Compressive Strength Test. After the specimens of solidified saline soil were subjected to standard curing to certain curing age, the unconfined compressive strengths (UCSs) of the specimens were measured under the curing ages 7, 14, 28, 56, 90, 180, and 360 days, as shown in Table 5. The UCS was tested under the controlled stress. The pressure increased step by step, and the specimens were maintained at a stress level to measure the vertical deformation of the specimens. After deformation stabilised, next-level load was applied to specimens until the specimens were damaged. The specimens were regarded as stable when the vertical deformation rate was less than 0.5 mm/min, and the loading rate was set to 0.20 kN/s. The specimens were regarded as being damaged when the stress remained unchanged while deformation increased; moreover, cracks were found in specimens.

2.2.2. Water Stability Test. The specimens of solidified soil were subjected to standard curing for 6 d, and then their UCS (f_{u2}) was measured. On the seventh day, the specimens were immersed in fresh water for 24 h and then their UCS (f_{u1}) was measured. The softening coefficient K of solidified soil could be calculated, where $K = (f_{u1}/f_{u2}) \times 100\%$.

2.2.3. Soluble Ion Contents. In our study, the specimens of solidified soil being subjected to standard curing for 56 d and 360 d were milled to powder. Afterwards, according to NY/T112.16-2006 *Detection of Soil*, the contents of soluble ions (Cl^{-1} and SO_4^{2-}) in specimens were measured.

Figure 2: Solidified soil samples.

2.2.4. SEM Analysis. SEM observation was performed to analyse the hydration products of the specimens using a Zeiss SUPRATM55 scanning electron microscope. The magnification range is 12~1000000x, and the acceleration voltage range is 0.02~30 kV. By utilising the ISM-6480LV SEM, the microstructures of solidified soil undergoing standard curing for 28 d were observed.

2.2.5. EDS Analysis. By employing the Noran System Six EDS, EDS energy spectral analysis for standard curing age 28 d was conducted on hydration products of solidified soil, and the chemical compositions of the hydration products were calculated through the SEM.

2.2.6. XRD Analysis. XRD analysis was carried out on specimens of solidified soil for standard curing age 28 d by using the D8 Advance XRD. The X-ray diffraction (XRD) spectra of the specimens were observed using a D/Max-RC diffractometer (Japan) with Cu Kα radiation, voltage of 40 kV, current of 150 mA, and 2 h scanning ranging between 5 and 90. The samples were manually grounded.

3. Test Results and Analysis

3.1. Mix Design. Liu [19] used calcium oxide and gypsum as the activator to activate the activity of mineral powder. Inspired by Liu, we used MgO as the activator. $Mg(OH)_2$ in lime was dissociated into magnesium and hydroxide ions. The diffusion layer of clay particles in soil mostly contained ions, *i.e.*, K^+ and Na^+, and then Ca^{2+} and Mg^{2+} ions in lime underwent exchange interactions with K^+ and Na^+ in the soil. As a result, the diffusion layer of the colloid was thinned to reduce the potential, and particles became more tightly bound, which strengthened the condensed structure of this lime-stabilised soil and reduced the dispersion, shrinkage, and expansivity. In this way, engineering properties of soil were improved. A certain amount of active MgO was added into Portland cement to realise shrinkage compensation by hydration of active MgO to $Mg(OH)_2$. The addition of MgO to cementitious composite materials is mainly to take advantage of the activity of MgO and microexpansive properties of $Mg(OH)_2$, so adjusting the proportion of MgO can enhance the strength of the cementitious composite materials. The schematic diagram for the improvement mechanism is shown in Figure 3.

Table 1: Chemical composition of contents of blast furnace slag (w_t%).

Compositions	SiO_2	Al_2O_3	Fe_2O_3	MgO	CaO	MnO	TiO_2	Loss on ignition
Content	34.46	13.00	3.21	8.64	38.00	0.29	0.84	0.68

Table 2: Properties of mineral powders.

Specific surface area (m^2/kg)	Water content (%)	Fluidity (%)	Activity ratio (%)	Density g/cm^3	Fineness (%)	SO_3 (%)	Cl^-(%)
50	0.26	96	76.9	2.8	6.1	2.01	0.032

Table 3: Main performance indices of cement.

Cement grade	Setting time (min)	Fineness (%)	Fineness (%)	Water requirement of normal consistency (%)
P·S·B32.5R	Initial set 150	Final set 240	8.2	28.1

Table 4: Component analysis of soluble salt in saline soil.

Item	K^+ (mg/kg)	Na^+ (mg/kg)	Ca^{2+} (mg/kg)	Mg^{2+} (mg/kg)	HCO_3^- (mg/kg)	Cl^-(mg/kg)	SO_4^{2-} (mg/kg)	pH
Value	283	6000	785	812	128	10250	2575	7.5

Table 5: Details of specimens.

Curing ages		7 d	14 d	28 d	56 d	90 d	180 d	360 d
Serial number of the specimens	Specimens solidified by the new cementitious composite materials	A-1	A-2	A-3	A-4	A-5	A-6	A-7
	Specimens solidified by cement	B-1	B-2	B-3	B-4	B-5	B-6	B-7

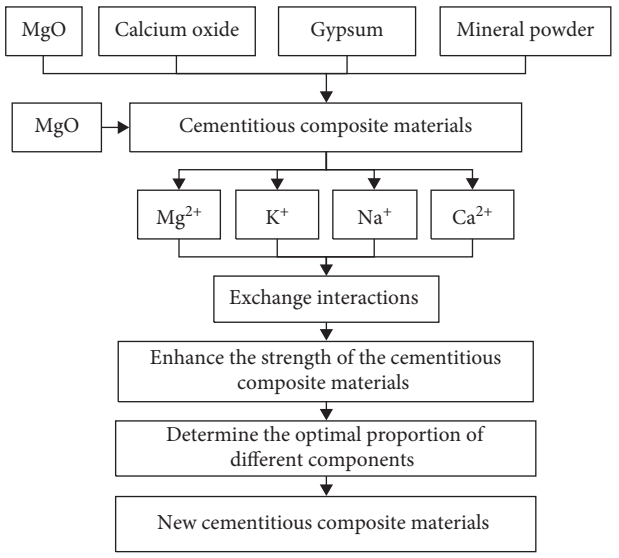

Figure 3: Schematic diagram for the improvement mechanism.

Owing to saline soil containing a high water content (30%) and there being no cement clinker used in the test, the activity of MgO and microexpansive properties of $Mg(OH)_2$ were fully employed. The proportions of MgO in the cementitious composite material were successively set to 4%, 5%, 6%, 7%, 8%, 9%, 10%, 11%, and 12%, respectively. By comparing strengths of the saline soil solidified by cementitious composite materials with different proportions of MgO, the optimal dose of MgO in the cementitious composite material was determined. The test blocks of the saline soil solidified by cementitious composite materials were cured for 7, 14, 28, 56, 90, 180, and 360 d, respectively. The proportions of the solidifying materials are listed in Table 6.

3.2. Determination of Optimal Proportions. In order to determine the optimal proportion of different components in the new cementitious composite materials, the influence of the different proportions of solidifying material on the strength of solidified saline soil was investigated, as shown in Table 6. Additionally, the amounts of the cementitious composite materials added in this solidified saline soil were separately set to 7%, 10%, 15%, and 20%, as shown in Figure 4.

It can be seen from Figure 4 that the UCS of the solidified saline soil all initially increased and then decreased at different curing ages with the increasing proportion of MgO. As the added amount of MgO was increased from 4% to 10%, the UCS of the solidified saline soil increased; as the added amount of MgO was increased from 10% to 12%, the UCS of the solidified saline soil decreased. Moreover, the growth in strength of solidified saline soil caused by increasing addition of MgO (from 4% to 10%) was more significant than the reduction of strength induced by decreasing addition of mineral powder. That is, the improvement of active and microexpansive effects of MgO mainly attributed to the growing addition amount of MgO. As the added amount of MgO was increased from 10% to

Table 6: Proportions of solidifying materials.

Serial number	MgO (%)	Calcium oxide (%)	Gypsum (%)	Mineral powder (%)
1	4	7.5	7.5	81
2	5	7.5	7.5	80
3	6	7.5	7.5	79
4	7	7.5	7.5	78
5	8	7.5	7.5	77
6	9	7.5	7.5	76
7	10	7.5	7.5	75
8	11	7.5	7.5	74
9	12	7.5	7.5	73
10			Cement	

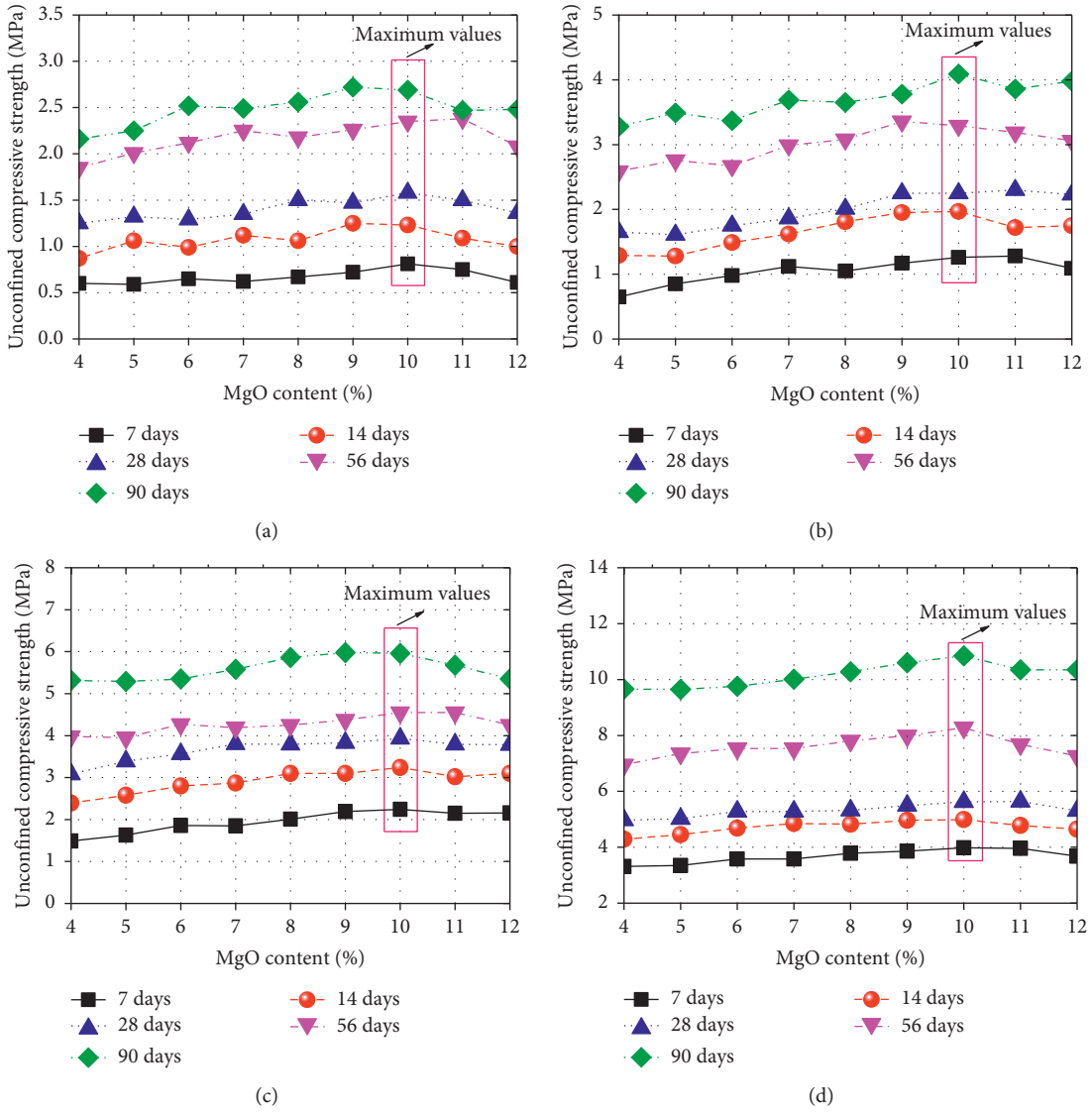

Figure 4: The influence of MgO content on the strength of solidified saline soil. (a) Adding 7% solidifying material. (b) Adding 10% solidifying material. (c) Adding 15% solidifying material. (d) Adding 20% solidifying material.

12%, the active effect of MgO increased while the active effect of mineral powders decreased. In this case, the large microexpansive effect of MgO caused the reduction of the solidified saline soil strength. With the addition of solidifying materials, the strength of solidified saline soil increased significantly. The optimal proportions of the

new cementitious composite materials were 75% mineral powders, 7.5% calcium oxide, 7.5% gypsum, and 10% active MgO.

3.3. Water Stability Test and Long-Term Strengths of the Solidified Saline Soil. According to the softening coefficient $K = (f_{u1}/f_{u2}) \times 100\%$, we can obtain the softening coefficients of the saline soil solidified by the new cementitious composite materials and cement (addition amounts 15%) at standard curing age 7 d, as shown in Table 7.

As shown in Table 7, the softening coefficient of the saline soil solidified by the new cementitious composite materials was greater than cement, which shows that the water stability of the saline soil solidified by the new cementitious composite materials is better than cement.

The use of the long-term UCS can save the engineering cost; thus, we investigated the UCS of the specimens at the curing ages 7, 14, 28, 56, 90, 180, and 360 d, and the specimens are cured through standard curing and immersion curing. The added amount of MgO in the cementitious composite materials was 10%, and the dosage of the new cementitious composite materials was 15%. The long-term UCS of the saline soil solidified by using the new cementitious composite materials and cement is shown in Figure 5.

It can be seen from Figure 5 that with the increase of the curing age from 7 d to 180 d, the growth rate of the strength of saline soil solidified by cements was greater than that solidified by the new cementitious composite material. When the curing age is 180 d, the UCS of the saline soil solidified by the new cementitious composite material began to be greater than that solidified by the cement through standard curing. When the curing age is 240 d, the UCS of the saline soil solidified by the new cementitious composite materials began to be greater than that solidified by the cement through immersion curing. Moreover, the test blocks of saline soil solidified by the new cementitious composite material were undamaged after being immersed in water. This indicated that the generated hydration products had coated the soil particles so that internal structure was compact, which allowed the solidified saline soil to resist damage. Therefore, with the increase of the curing ages, the strength of the saline soil solidified using two solidifying materials increased. However, when reaching certain curing age, the strength of the saline soil solidified by the cement increased very slowly, and the strength of the saline soil solidified by the new cementitious composite materials also increased fast. The long-term strength of saline soil solidified using the new cementitious composite material was greater than that of saline soil solidified using cement.

3.4. Analysis of Soluble Salts. The soluble salts in saline soil solidified using the cement and the new cementitious composite materials (added amount, 15%) were separately analysed. Table 8 listed the water-soluble ion contents and pH of the saline soil solidified using the two types of solidifying materials.

Table 7: Test result of the water stability of solidified soil.

Solidified material	f_{u1} (MPa)	f_{u2} (MPa)	K
New cementitious composite materials	5.12	5.45	0.94
Cement	5.20	5.74	0.91

It can be seen from Table 8 that saline soil approximated to neutral soil. After adding solidifying materials, cement was hydrated to generate $Ca(OH)_2$ while CaO in the added new cementitious composite materials reacted with H_2O to generate $Ca(OH)_2$, and the soil became alkaline. With the increase of the curing age, the soil pH decreased. Owing to active MgO being added to the new cementitious composite materials, the Mg^{2+} content in saline soil solidified using the new cementitious composite materials was always much greater than that in saline soil solidified using cement; however, the Mg^{2+} content in saline soil solidified using the new cementitious composite materials decreased with prolonged curing age. The main reason for this was that active MgO was subjected to a hydration reaction under the effect of soluble Mg^{2+} and Cl^-, and the hydration reaction generated $5Mg(OH)_2{\cdot}MgCl_2{\cdot}8H_2O$ and $Mg(OH)_2{\cdot}MgCl_2{\cdot}8H_2O$. On the other hand, active MgO reacted with H_2O to generate $Mg(OH)_2$. Owing to the solubility of $Mg(OH)_2$ being lower than that of $Ca(OH)_2$, Mg^{2+} preferentially reacted with OH^- to generate $Mg(OH)_2$, which replaced $Ca(OH)_2$ in mineral powders to react with active SiO_2 as follows: $Mg(OH)_2 + SiO_2 \longrightarrow$ M-S-H. The contents of soluble salt ions Na^+ and Cl^- in saline soil solidified using cement and the new cementitious composite materials both greatly decreased with the increase of curing age. This indicated that the two types of solidifying materials exhibited a favourable solidifying effect on harmful ions in saline soil. Moreover, the capacity of the new cementitious composite materials for solidifying Cl^- was stronger than that of cements as active MgO was subjected to a hydration reaction under the effect of soluble Mg^{2+} and Cl^- to generate $5Mg(OH)_2{\cdot}MgCl_2{\cdot}8H_2O$ and $3Mg(OH)_2{\cdot}MgCl_2{\cdot}8H_2O$. Thus, a certain amount of Cl^- was absorbed by active MgO added to the new cementitious composite material so that the capacity of the material for solidifying Cl^- was stronger than that of cement.

3.5. XRD Analysis. By conducting XRD analysis on hydration products of the new cementitious composite materials, the compositions of hydration products can be determined. Chemically pure NaCl was added into the new cementitious composite materials (taking up 2% of the material), and the test blocks composed entirely of the new cementitious composite materials cured for 28 d were prepared. In this way, the mechanism of the new cementitious composite materials cured for Cl^- was investigated. Figure 6 shows the test result obtained through XRD analysis.

As shown in Figure 6, A and B refer to the main diffraction peaks of SiO_2 and Friedel salts ($3CaO{\bullet}Al_2O_3{\bullet}CaCl_2{\bullet}10H_2O$), respectively; C denotes the main

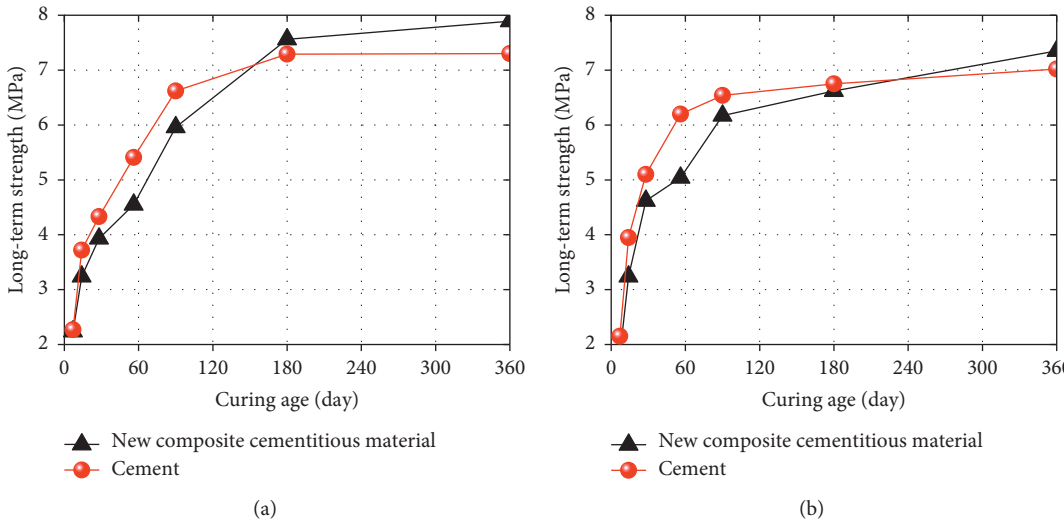

Figure 5: Long-term strengths of saline soil solidified by using the new cementitious composite materials and cement. (a) Standard curing. (b) Curing in fresh water.

Table 8: Water-soluble salt ion contents and pH.

Sample	pH	Na^+ (mg/kg)	Cl^- (mg/kg)	Ca^{2+} (mg/kg)	Mg^{2+} (mg/kg)	SO_4^{2-} (mg/kg)
Saline soil	7.6	4830	8830	1080	308	1765
Soil solidified using the cement for 56 d	10.7	3426	4152	385	51	416
Soil solidified using the cement for 360 d	9.6	727	1064	131	3	329
Soil solidified using the new cementitious composite material for 56 d	11.4	2900	3335	596	565	684
Soil solidified using the new cementitious composite material for 360 d	10.5	639	798	226	36	209

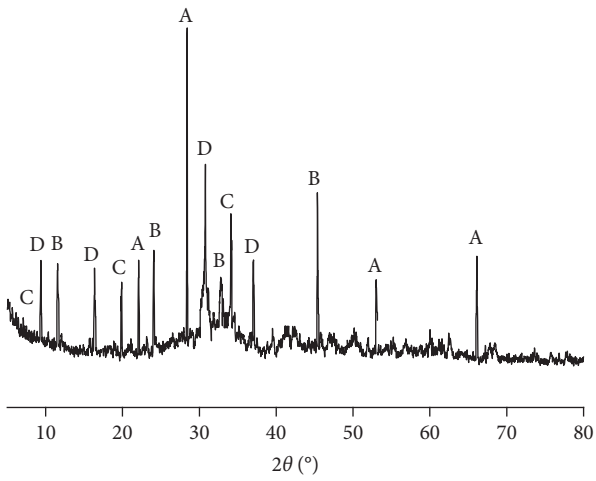

Figure 6: XRD result of the hydration product.

diffraction peak of AFm ($3CaO•Al_2O_3•CaSO_2•12H_2O$), and D represents the main diffraction peak of AFt ($3CaO•Al_2O_3•3CaCO_3•12H_2O$). According to XRD spectra, it can be found that AFt, AFm, and Friedel salts were generated in hydration products. Similarly, these compounds were also generated when solidifying saline soil using the new cementitious composite materials. This indicated that the use of the new cementitious composite materials not only solidified saline soil to endow the soil with certain strength but also absorbed Cl^- to reduce the harm.

3.6. SEM Analysis. The microstructures of the saline soil solidified using the cement and the new cementitious composite materials (added amount, 15%) after standard curing 28 d and 360 d were investigated, as shown in Figures 7 and 8.

As shown in Figures 7 and 8, the internal structure of saline soil solidified by applying the new cementitious composite materials for 28 d was compact: soil particles, the microstructure of the saline soil, were uniformly distributed, and they were surrounded by the cementitious materials, which are our newly developed cementitious composite materials. Although the water content in test blocks reached 30%, the internal structure of the test blocks did not show significant defects, *i.e.*, gaps, holes, and fractures. As a result, there was low possibility for the relative motion under the effect of external force, thus effectively improving the strength and stiffness of the solidified soil. By contrast, the internal structure of saline soil solidified by the cements for 28 d was loose: significant gaps and holes were found

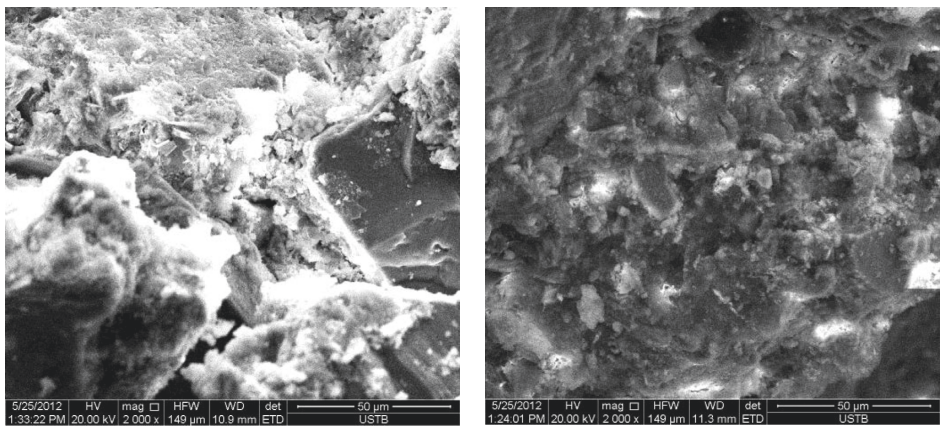

(a) (b)

Figure 7: SEM analysis of saline soil solidified using the two solidifying materials after standard curing 28 d. (a) Solidification using cement. (b) Solidification using our improved material.

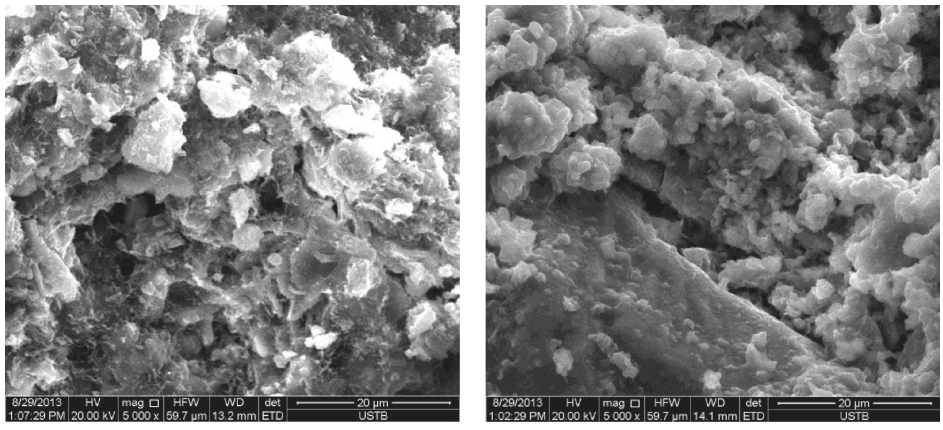

(a) (b)

Figure 8: SEM analysis of saline soil solidified by using cement and the cementitious composite material after standard curing 360 d. (a) Solidification using cement. (b) Solidification using our improved material.

between cementing agents and soil particles. After standard curing for 360 d, the saline soils solidified by using the two types of solidifying materials were both compact: soil particles were surrounded by hydration products and there were many clustered and petal-shaped C-S-H gels as well as flaky hydration products present. The main reason for this was that ettringite, Aft, and AFm were interactively crossed so that soil particles were less likely to be in relative motion, which was also the reason why the strength of the saline soil increased with prolonged curing time.

3.7. EDS Analysis. By conducting EDS, the chemical compositions of solidified saline soil can be determined. Therefore, when adding 15% of the new cementitious composite materials, the chemical compositions of the solidified saline soil for standard curing (28 d) were measured by SEM-EDS, as shown in Figure 9 and Table 9.

It can be seen from Figure 9 and Table 9 that Ca/Si in C-S-H gels was mostly between 0.8 and 2.0 at%. Therefore, it was supposed that Si was completely transformed into a C-S-H gel with Ca/Si = 1.5.

Then, subtracting atomic numbers of Si and Ca, the percentage contents of atomic numbers of the remaining elements (Al, Cl, and Ca) were calculated, as shown in Table 10.

As shown in Table 10, the ratios of Al : Cl : S : Ca at measurement points 1 and 2 were 1 : 0.57 : 0.09 : 1.77 and 1 : 0.54 : 0.13 : 1.80, respectively. The ratio (Al : Cl : Ca) of atomic numbers in Friedel salt ($3CaO{\bullet}Al_2O_3{\bullet}CaCl_2{\bullet}10H_2O$) was 1 : 1:2 while the ratio (Al : S : Ca) of atomic numbers in AFm ($3CaO{\bullet}Al_2O_3{\bullet}CaSO_4{\bullet}12H_2O$) was 1 : 0.5 : 2. Therefore, it can be determined that measurement points 1 and 2 separately denoted mixtures of AFm and Friedel salt. Chloroaluminate ($3CaO{\bullet}Al_2O_3{\bullet}CaCl_2{\bullet}10H_2O$) formed by using Cl^- and mineral admixture, also called Friedel salt, was a type of AFm series. The AFm series contained multiple compounds, and the typical compounds included $3CaO{\bullet}Al_2O_3{\bullet}CaCl_2{\bullet}nH_2O$, $3CaO{\bullet}Al_2O_3{\bullet}CaSO_4{\bullet}nH_2O$, and $3CaO{\bullet}Al_2O_3{\bullet}CaCO_3{\bullet}nH_2O$. In practical hydration

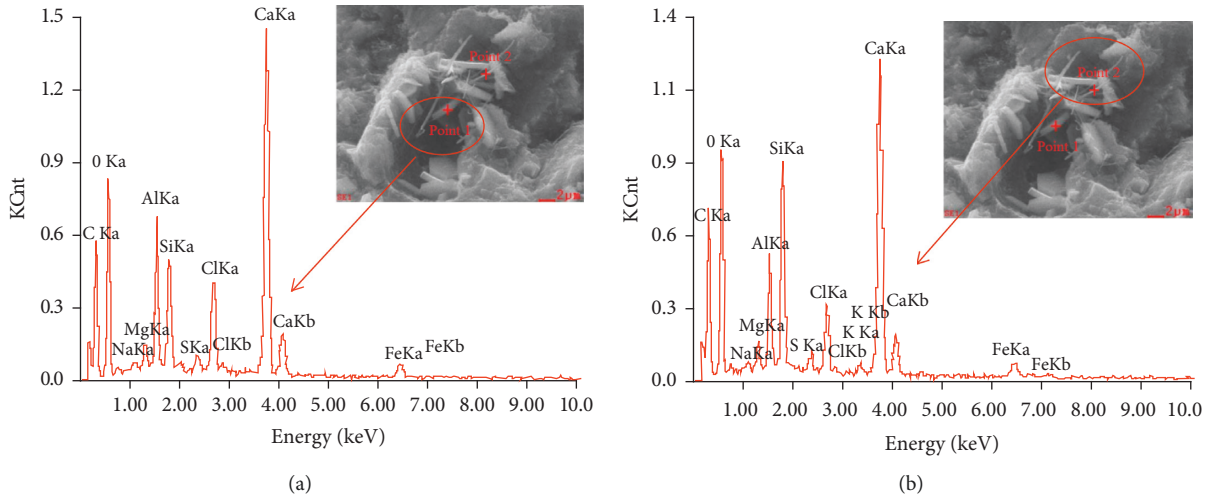

Figure 9: EDS analysis of the new cementitious composite material. (a) Point 1. (b) Point 2.

Table 9: EDS analysis result: points 1 and 2.

Element	O	Na	Mg	Al	Si	S	Cl	Ca	Fe
Point 1 (at%)	35.03	0.39	0.82	3.84	3.19	0.36	2.20	9.79	0.81
Point 2 (at%)	34.55	0.33	0.74	2.71	4.87	0.35	1.47	8.24	0.74

Table 10: Calculated chemical compositions: points 1 and 2.

Test point	Composition	O (%)	Na (%)	Mg (%)	Al (%)	Si (%)	S (%)	Cl (%)	Ca (%)	Fe (%)
Point 1	Percentage content of atomic number	35.03	0.39	0.82	3.84	3.19	0.36	2.2	11.58	0.81
	Si and Ca in C-S-H gel	—	—	—	—	3.19	—	—	4.79	—
	Percentage content of residual atomic number	35.03	0.39	0.82	3.84	0	0.36	2.2	6.80	0.81
	Percentage of atomic number	—	—	0.21	1.00	0.00	0.09	0.57	1.77	0.21
Point 2	Percentage content of atomic number	34.55	0.33	0.74	2.71	4.87	0.35	1.47	12.19	0.74
	Si and Ca in C-S-H gel	—	—	—	—	4.87	—	—	7.31	—
	Percentage content of residual atomic number	34.55	0.33	0.74	2.71	0.00	0.35	1.47	4.89	0.74
	Percentage of atomic number	—	—	0.27	1.00	0.00	0.13	0.54	1.80	0.27

processes, due to co-occurrence of multiple ions, several compounds which were likely to appear as synchronously or complex compounds containing multiple ions that can replace each other were generated; however, no matter which type of compounds was generated, the new cementitious composite material showed an excellent capacity for chemically bonding Cl^-. By analysing the molecular formula of the hydration products, it can be found that the Cl^- in saline soil can be eliminated through reaction with the material, which was the fundamental reason why the content of free Cl^- in saline soil declined with increase of the curing time. By calculating the volumes of various reactants and products before and after generation of $3CaO{\bullet}Al_2O_3{\bullet}CaCl_2{\bullet}10H_2O$, it was found that the volume of solid phase increased by about 76% during the generation of $3CaO{\bullet}Al_2O_3{\bullet}CaCl_2{\bullet}10H_2O$. It can also be seen that saline soil solidified using the new cementitious composite materials was more compact through SEM; therefore, the solid phase expanded when generating $3CaO{\bullet}Al_2O_3{\bullet}CaCl_2{\bullet}10H_2O$ to fill pores in the soil, which was also one of reasons why $CaO{\bullet}Al_2O_3{\bullet}CaCl_2{\bullet}10H_2O$ can increase the strength of the solidified soil.

4. Engineering Application in the Saline Soil Subgrade Strengthening

4.1. Finite Element Model of the Subgrade. In this section, we built the numerical simulation model to evaluate the seismic performance of the saline soil subgrade. The saline soil subgrade engineering of our study is located near the Sichuan-Tibet railway in China, which is under construction, as shown in Figure 10. Our research group drilled lots of boreholes in our survey region. The seismic activity around Sichuan-Tibet railway is relatively frequent. The groundwater level which changes with the season is commonly above 2.0 m.

In 2018, there have been more than eighty small earthquakes in Tibet Province while there were more than thirty small earthquakes in Sichuan Province. Soil salinization phenomenon is widespread in our survey region, and the saline soil often caused cracking and settlement of the subgrade under the

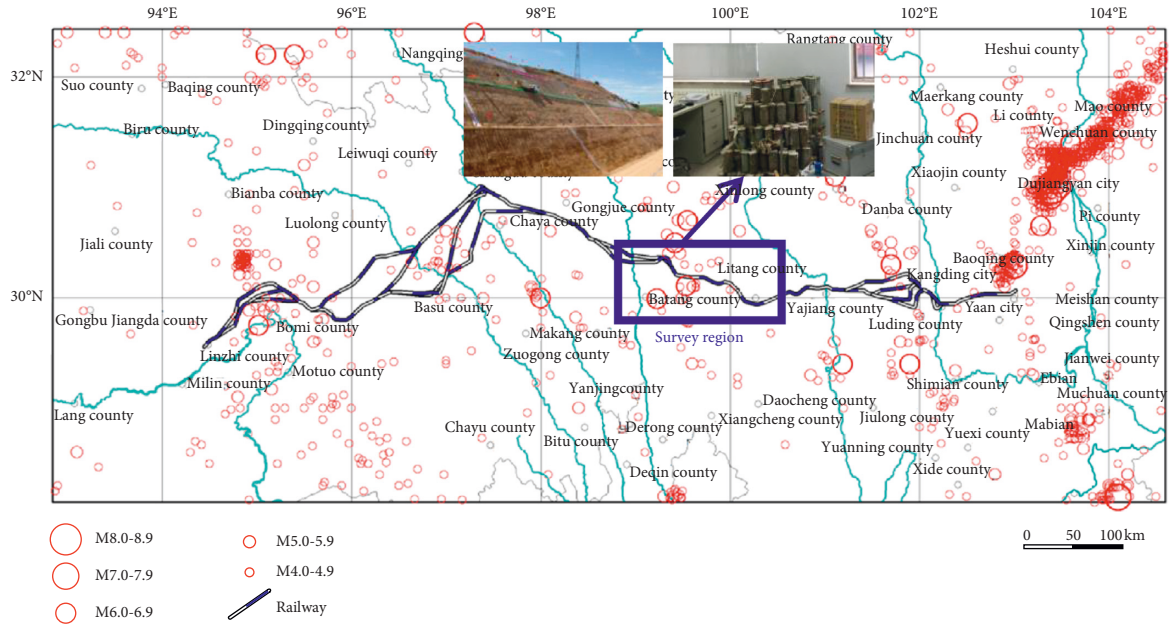

Figure 10: Geographic position of the survey region and seismic epicentral distribution map.

influence of the earthquake and rainfall. Consequently, a new composite cementing material for saline soil was developed by us to strengthen the subgrade, and a good effect of strengthening was achieved, as shown in Figure 11.

The slope models are established with finite element software MIDAS GTS NX, and we have simplified the slope models to some extent. The length of the model is 100 m, and the height of the model is 25 m. The subgrade width is 4.2 m, the right slope height of the subgrade is 6 m, and the left slope height is 20 m. In order to guarantee the accuracy of the calculation, the maximum size of the grid is less than 1/10~1/8 of the shortest wavelength of the input seismic waves. The Mohr–Coulomb elastic-plastic model is used to model the stress-strain behaviour of the soil. The grid size of the numerical simulation model is 0.5 m, and there are 5000 elements, as shown in Figure 12. Furthermore, the left, right, and bottom boundaries are set as viscoelastic artificial boundaries.

In the numerical simulation model, the quality damping coefficient α and the stiffness damping coefficient β are fixed as 0.2 and 0.0019, respectively. So, the damping coefficient of the numerical simulation model is calculated by the Rayleigh damping formula, as illustrated in the following equation:

$$[C] = \alpha[M] + \beta[K], \tag{1}$$

where α is the quality damping coefficient and β is the stiffness damping coefficient. Moreover, the quality damping coefficient and the stiffness damping coefficient are computed by the following equations:

$$\alpha = \frac{2\omega_i\omega_j\left(\xi_i\omega_j - \xi_j\omega_i\right)}{\omega_j^2 - \omega_i^2},$$
$$\beta = \frac{2\left(\xi_i\omega_j - \xi_j\omega_i\right)}{\omega_j^2 - \omega_i^2}, \tag{2}$$

where ω_i represents the natural frequency of the first model, ω_j corresponds to the natural frequency of the second model, and the range of the conventional damping ratios ξ_i and ξ_j are 2%~7%.

Based on the indoor experiment including the dynamic triaxial test and consolidation test, the physical parameters of the subgrade materials are shown in Table 11.

4.2. Selection of the Seismic Waves. The basic seismic intensity of the region of the subgrade is 7 degrees, and the site is II. According to *Code for Seismic Design of Railway Engineering (GB50111-2006)* [20] of China, the basic acceleration value of severe earthquake is 0.21 g, as shown in Table 12.

The El Centro earthquake, which happened in Imperial County, California, in the United States in 1940, is used in our study, as shown in Figure 13, and the peak accelerations of the seismic waves are adjusted for 0.21 g, as shown in Table 10. The acceleration time histories of the seismic wave are shown in Figure 9. Because the failure of the subgrade is mainly affected by the horizontal earthquake, only the influence of horizontal earthquake on the subgrade is considered.

4.3. Seismic Dynamic Response of Subgrade before and after Solidification. In order to determine the seismic dynamic response of the subgrade before and after strengthening using our newly developed cementitious composite material, we investigated the change laws of displacement, acceleration, and excess pore water pressure of the subgrade under the El Centro earthquake, which are the main index of reflecting the seismic resistant performance of the subgrade. The settlement and right slope stability of the subgrade are our main focus location in engineering, and we set the

(a) (b)

(c)

Figure 11: Solidification of the saline soil in the subgrade.

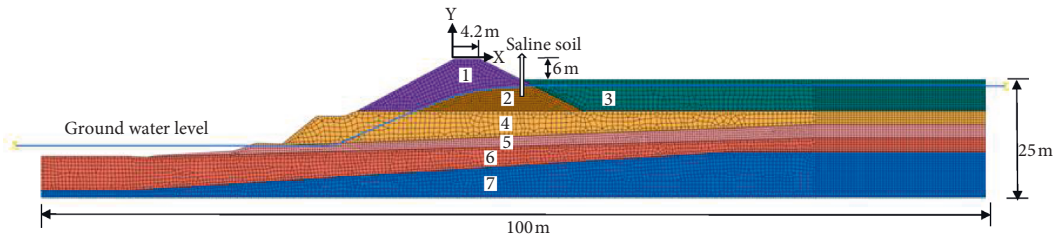

Figure 12: Calculation model of the subgrade. 1, subgrade filling; 2, saline soil; 3 and 5, silty soil; 4 and 6, silty clay soil; 7, weathered rock.

Table 11: Physical parameters of the subgrade.

Soil	Poisson's ratio	Elastic modulus (MPa)	Gravity ($kN \cdot m^{-3}$)	Cohesion (kPa)	Friction angle (°)	Initial void ratio	Coefficient of permeability ($cm \cdot s^{-1}$)
Material 1	0.38	100	15	32	24	0.85	$1e-5$
Material 2 (before solidification)	0.35	120	16	18	33	0.80	$1e-6$
Material 2 (after solidification)	0.27	320	19	50	38	0.40	$4e-9$
Material 3	0.32	129	17	35	26	0.78	$2e-6$
Material 4	0.3	185	16	35	34	0.75	$5e-7$
Material 5	0.28	274	18	45	35	0.65	$6e-7$
Material 6	0.25	756	20	65	30	0.50	$7e-9$
Material 7	0.21	975	21.2	80	32	0.40	$1e-10$

Table 12: Basic earthquake acceleration value in Chinese code.

Earthquake category	6 degrees	7 degrees	8 degrees	9 degrees
Frequent earthquake	0.02 g	0.04 g	0.07 g	0.14 g
Rare earthquake	0.11 g	0.21 g	0.38 g	0.64 g

subgrade top as the monitoring line 1 and the right slope of the subgrade as line 2. Also, the subgrade is often damaged by the excess pore water pressure during earthquake, and we set four monitoring points in different heights of the saline soil, as shown in Figure 14.

First, we compute the settlement displacement of the subgrade top and the horizontal displacement of the right slope of the subgrade before and after strengthening, as shown in Figure 15.

As shown in Figure 15, it can be found that the maximum settlement displacement is 0.095 m before strengthening while the maximum settlement displacement is 0.03 m after strengthening, and the settlement displacement of the subgrade after solidification is 3.2 times less than that before solidification. Consequently, our developed materials used in saline soil subgrade strengthening achieved good results.

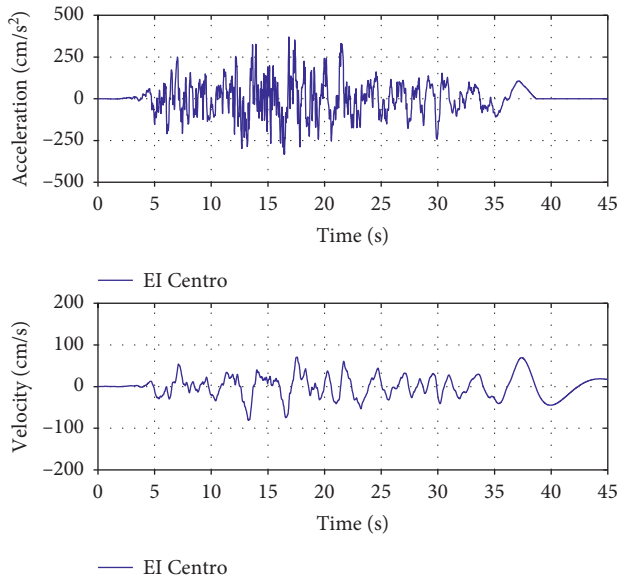

Figure 13: El Centro seismic wave.

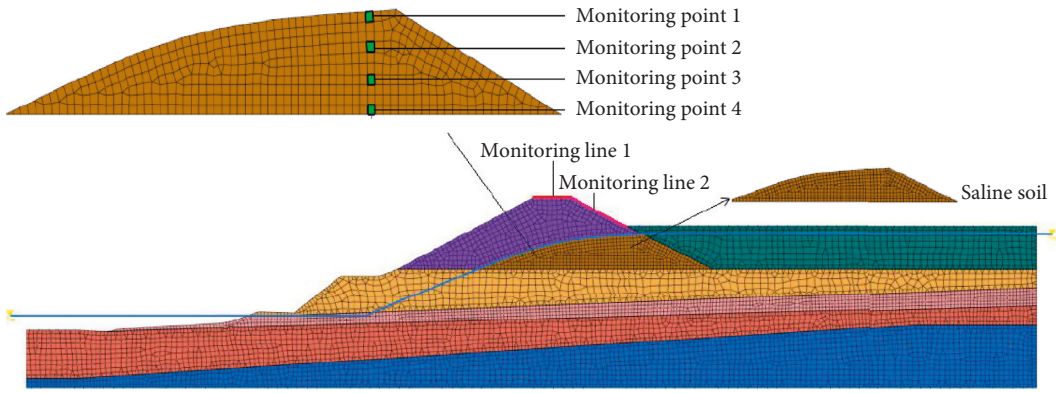

Figure 14: Monitoring lines and monitoring points of the model.

The horizontal displacement of the subgrade slope can determine whether the slope slides or not, and we found that the maximum horizontal displacement of the right slope after solidification is 1.7 times less than that before solidification, which shows that our developed materials can not only reduce the settlement deformation but also control the horizontal displacement of roadbed slope.

Since earthquake is dynamic load, the displacement is constantly changing under earthquake action, and the time at which the maximum deformation occurs can be quickly determined by observing the displacement time history; thus, the displacement time histories of the right slope top and slope toe are given as shown in Figure 16.

As shown in Figure 16, it can be seen that the displacement keeps fluctuating and accumulating under earthquake action, and the subgrade generated the permanent displacement, which shows that the subgrade produced the plastic deformation. The plastic deformation of the subgrade after solidification is less than that before solidification.

The contour of the maximum displacement is presented, and we can more intuitively observe the displacement changes of the subgrade before and after the strengthening, as shown in Figure 17.

As shown in Figure 17, we can see that the displacement of the subgrade top is the greatest under earthquake because of the dynamic amplification effect. However, the maximum displacement of the subgrade before strengthening is 5.09 cm while the maximum displacement of the subgrade before strengthening is 4.22 cm. The maximum displacement decreases 17%. Thus, our newly developed cementitious composite materials have good solidification effect on the subgrade deformation.

Through the above analysis, we can conclude that our developed materials have achieved good results in inhibiting the deformation of the saline soil subgrade under earthquake. Acceleration is another important index of the seismic performance of subgrade, and we also compute the horizontal accelerations of the subgrade top and the right slope of the subgrade before and after strengthening, as shown in Figure 18.

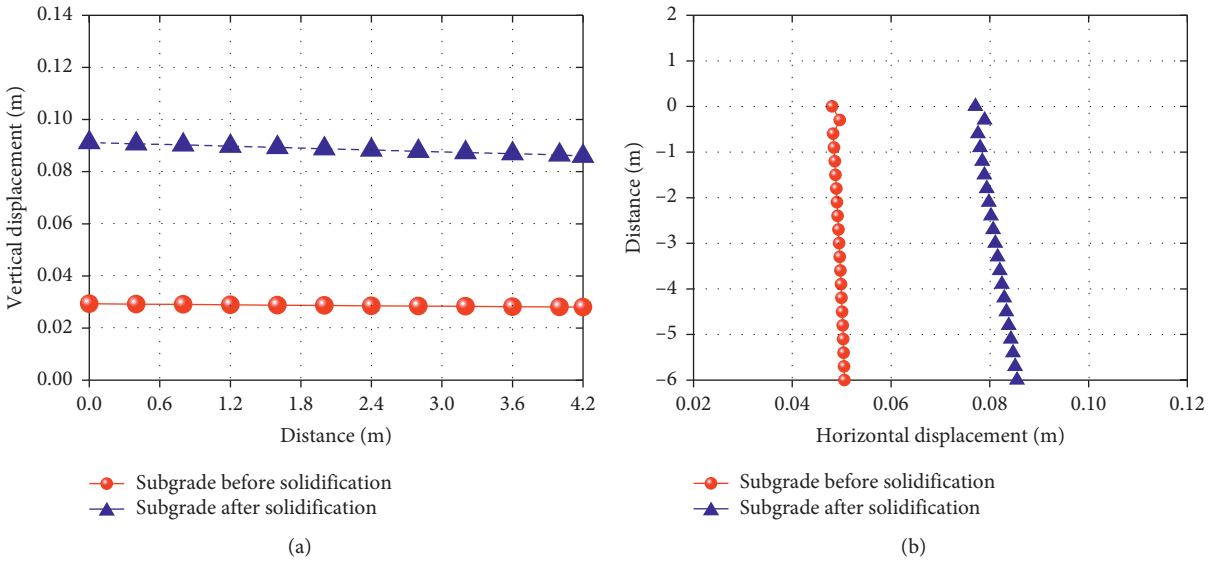

Figure 15: Settlement displacement of the subgrade top and the horizontal displacement of the right slope. (a) Subgrade top. (b) The right slope.

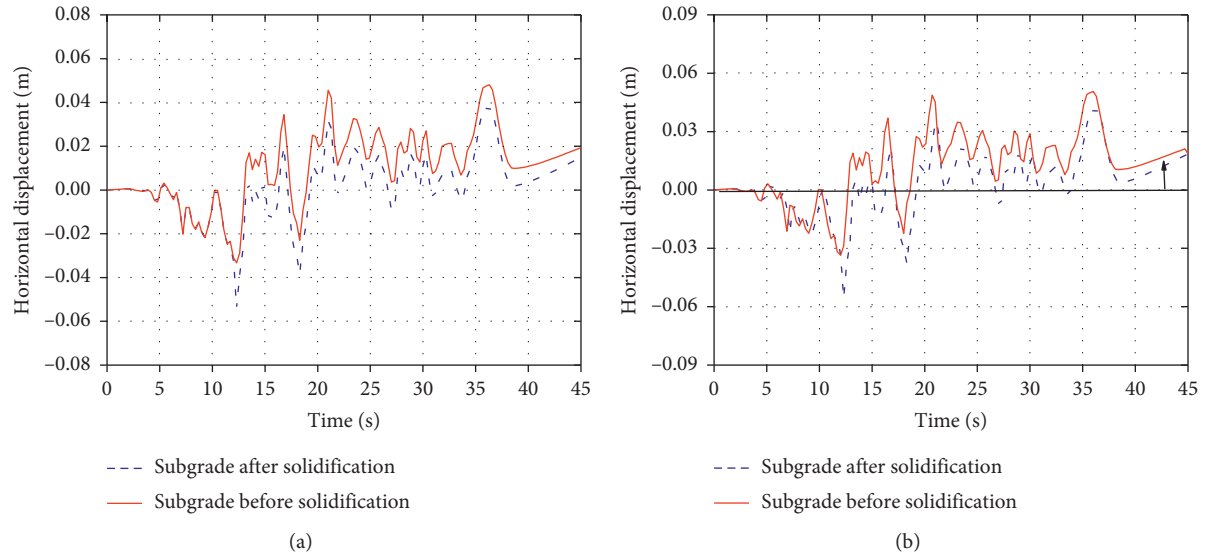

Figure 16: Displacement time histories of the right slope top and slope toe. (a) Slope top. (b) Slope toe.

As shown in Figure 18, we can see that the maximum accelerations of the subgrade top and the right slope after strengthening are less than those before strengthening, which shows that the solidification material can play a role in passive energy dissipation. The maximum acceleration of the subgrade top after strengthening decreases 1.1 times than that before solidification; while the maximum acceleration of the subgrade top after strengthening decreases 1.2 times than that before strengthening. Consequently, our newly developed cementitious composite materials not only have good solidification effect on the subgrade deformation but also have good solidification effect in passive energy dissipation control.

The acceleration is constantly changing under earthquake action, and the time at which the maximum acceleration occurs can be quickly determined by observing the acceleration time history; thus, the acceleration time histories of the right slope top and slope toe are given as shown in Figure 19.

As shown in Figure 19, we can see that the maximum acceleration of the right slope top is greater than that of the right slope toe under earthquake. The maximum accelerations are 2.92 m/s^2 and 2.34 m/s^2 of the right slope top before and after strengthening, respectively, while the maximum accelerations are 2.46 m/s^2 and 2.07 m/s^2 of the right slope toe before and after strengthening, respectively. Taking the right slope top as the example, the dynamic amplification factors are 1.47 and 1.2, which shows that the soil can amplify the seismic waves and the dynamic response of the subgrade is amplified by soil mass. In addition, our newly

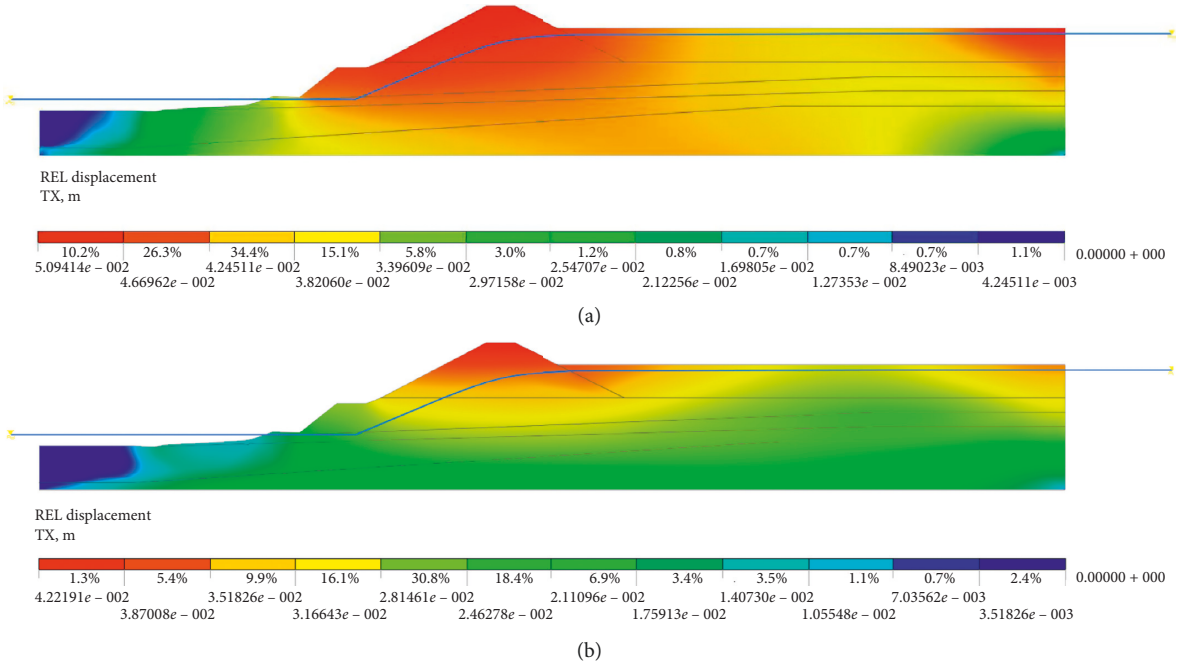

Figure 17: Displacement contour of the subgrade before and after strengthening. (a) Displacement contour of the subgrade before strengthening. (b) Displacement contour of the subgrade after strengthening.

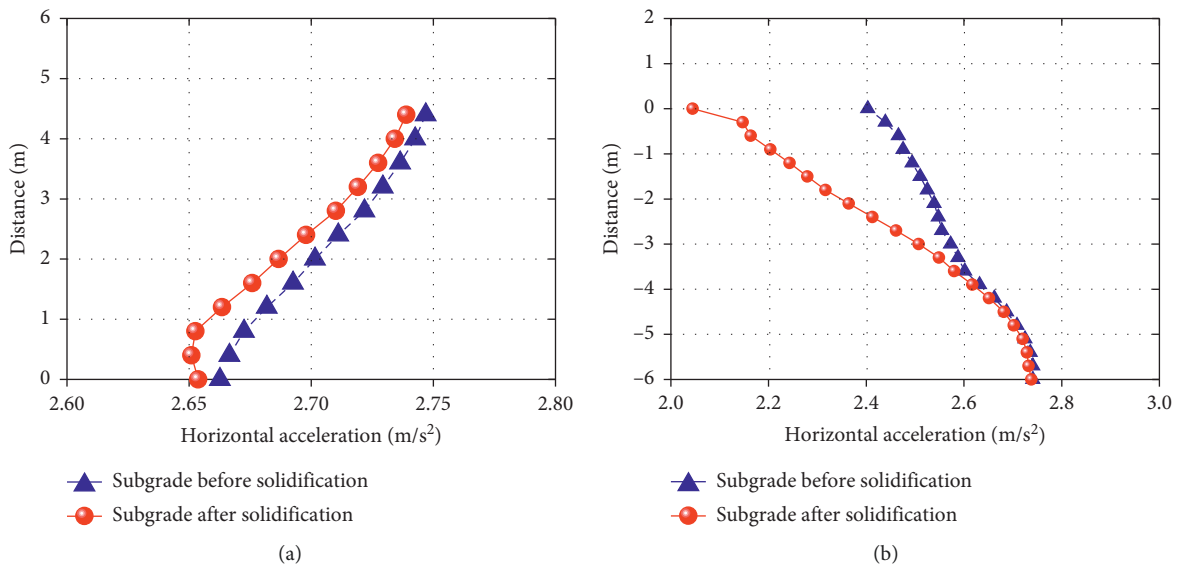

Figure 18: Horizontal accelerations of the subgrade top and the right slope of the subgrade before and after strengthening. (a) Subgrade top. (b) The right slope.

developed cementitious composite materials can not only strengthen the subgrade but also reduce the subgrade vibration under earthquake to ensure the traffic safety.

The main influencing factors of soil failure are the sharp increase of excess pore water pressure and the decrease of effective stress. Consequently, excess pore water pressure ratios of the saline soil before and after strengthening are investigated, as shown in Figure 20.

As shown in Figure 20, we can find that the excess pore water pressure ratio increases with the continuing effects of earthquakes. The excess pore water pressure ratios of the unstrengthened subgrade are greater than those of the strengthened subgrade. The maximum excess pore water pressure ratio of the unstrengthened subgrade is 0.82 while the maximum excess pore water pressure ratio of the strengthened subgrade is 0.65. Also, it can be seen that the excess pore water pressure of the unstrengthened subgrade continues to rise while the strengthened subgrade gradually dissipates, which shows that the excess pore water pressure dissipates fast.

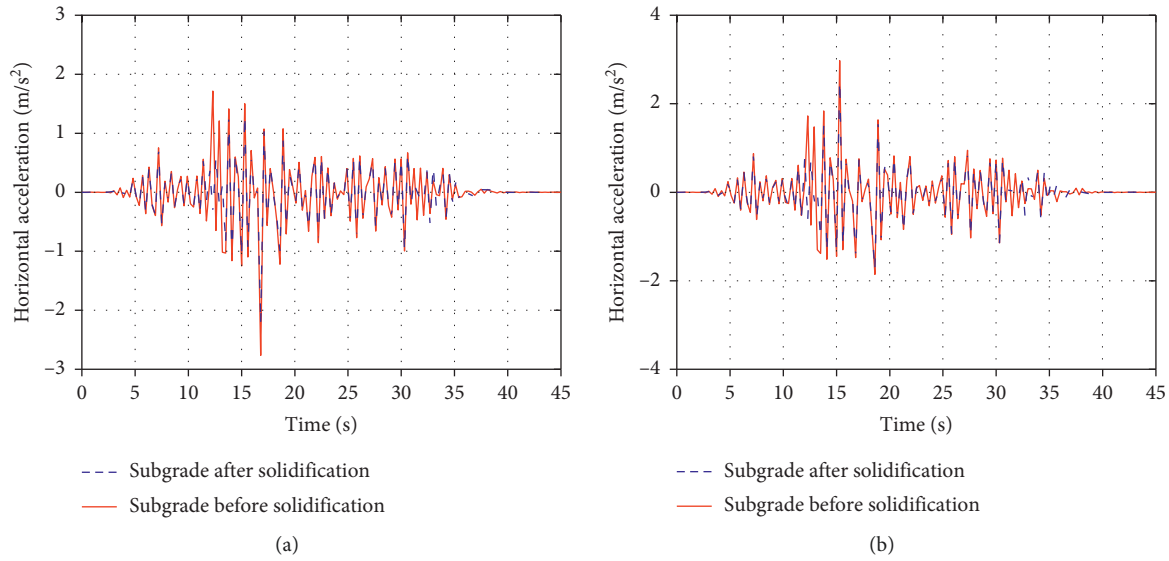

Figure 19: Horizontal acceleration time histories of the right slope top and slope toe. (a) Slope top. (b) Slope toe.

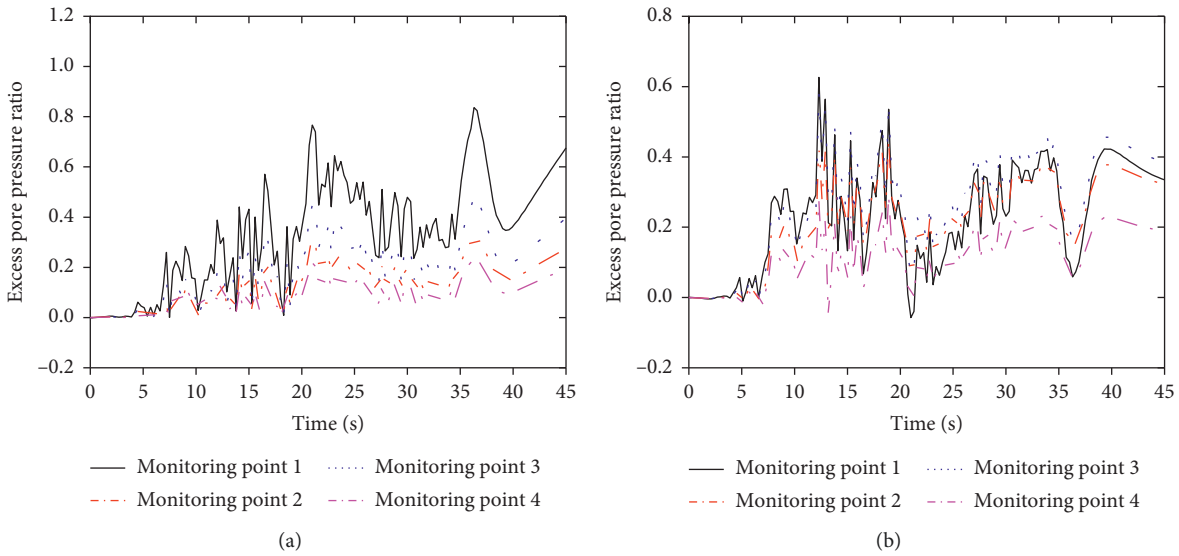

Figure 20: Excess pore water pressure ratios of the saline soil before and after strengthening. (a) Solidified subgrade. (b) Unsolidified subgrade.

4.4. Failure Modes of the Subgrade before and after Strengthening. We use the shaking table test which could reproduce the failure process of the subgrade under the real earthquakes to see the failure modes of the subgrade before and after strengthening. Figure 21 shows the shaking table test equipment to model the slope failure process under the seismic excitation.

As can be seen in Figure 21, the main technical indicators of the shaking table test equipment include rated working frequency (40 Hz), the maximum acceleration (20 m/s^2), the maximum test load (5000 kg), and dimensions of the shaking table (1.5 m × 1.5 m).

The size of the test model is 2 m × 1 m × 1.4 m. The slope rate of the subgrade is 1 : 1.5. To keep the soil uniform, the subgrade is repeatedly stirred. The sponge whose thickness is 20 m is to reduce the reflection of seismic waves at the border of the subgrade. The test model is shown in Figure 22.

The scaling law between our test model and the actual projects follow the Buckingham Pi theorem [21], and the proportional relation for the similarity ratio is developed by Jiang et al. [22]. Poisson's ratio μ of the soil in the test is 0.35, the coefficient $K = \mu/(1-\mu)$ of the lateral pressure is 0.54, and the dimensionless index $n = 2$. Other similarity coefficients based on similarity principle are shown in Table 13.where σ_v is the normal pressure stress (*i.e.*, the geostatic stress caused by burial depth); φ is the internal friction angle; c is cohesion; and k is the lateral pressure coefficient.

(a) (b) (c)

Figure 21: Shaking table test equipment. (a) Hydraulic system. (b) Shaking table. (c) Vibration controller.

(a) (b) (c)

Figure 22: Test model of the slope. (a) Geometric model. (b) Test model. (c) Rainer.

Table 13: Similarity coefficient between our test model and the actual projects.

Physical quantity	Similarity coefficient	Exegesis
Geometric dimensioning L	C_L	Control variable
Acceleration a	$C_a = C_{[\tau]}C_\rho^{-2/n}C_L^{-1}$	Control variable
Time T	$C_T = C_K^{-1/2}C_\rho^{1/2n}C_L^{2n-1/2n}$	Control variable
Density ρ	$C_\rho = 1$	
Strain level $\gamma/\overline{\gamma}$	$C_{(\gamma/\overline{\gamma})} = 1$	
Dynamic displacement u	$C_u = C_{[\tau]}C_K^{-1}C_\rho^{-1/n}C_L^{n-1/n}$	
Vibration velocity v	$C_v = C_u/C_T = C_{[\tau]}/C_K^{-1/2}C_\rho^{-(3/2n)}C_L^{-(1/2n)}$	
Vibration frequency w	$C_w = 1/C_T = C_K^{1/2}C_\rho^{-(1/2n)}C_L^{-(2n-1/2n)}$	
Damping ratio λ	$C_\lambda = 1$	
Dimensionless index n	$n = 2$	

$[\tau]$ is the horizontal shear strength and $[\tau]$ is computed by equation (3).

$$[\tau] = \sqrt{\left(\frac{1+k}{2}\sigma_v \sin\varphi + c\cos\varphi\right)^2 - \left(\frac{1-k}{2}\sigma_v\right)^2}, \quad (3)$$

In our experiment, similar material was developed based on the subgrade material. The similarity coefficients simulating the subgrade are shown in Table 14.

Next, we can more directly determine the failure degree of the subgrade before and after strengthening through the shaking table test, as shown in Figure 23.

As can be seen in Figure 23, through the shaking table test, we can more directly determine the failure degree of the subgrade before and after strengthening. Before strengthening, the destruction begins at the subgrade toe and the cracks in the subgrade spread gradually. Meanwhile, the position at the top of subgrade has obvious settlement phenomenon after earthquake. The sliding surface is approximately circular in shape. After strengthening, the destruction also begins at the subgrade toe, and the subgrade does not slip, while there are only a few cracks. Also, we found that the subgrade does not undergo subsidence deformation, which shows that our newly developed cementitious composite materials had a better strengthening effect.

Table 14: Similarity coefficients.

Physical quantity	Similarity constants
Dynamic shear strength (MPa)	4.85
Length (m)	6.00
Density (kg/m^3)	1.00
Acceleration (m/s^2)	0.81
Time (s)	2.72
Strain	1.00
Dynamic displacement (m)	51.56
Frequency (Hz)	0.19

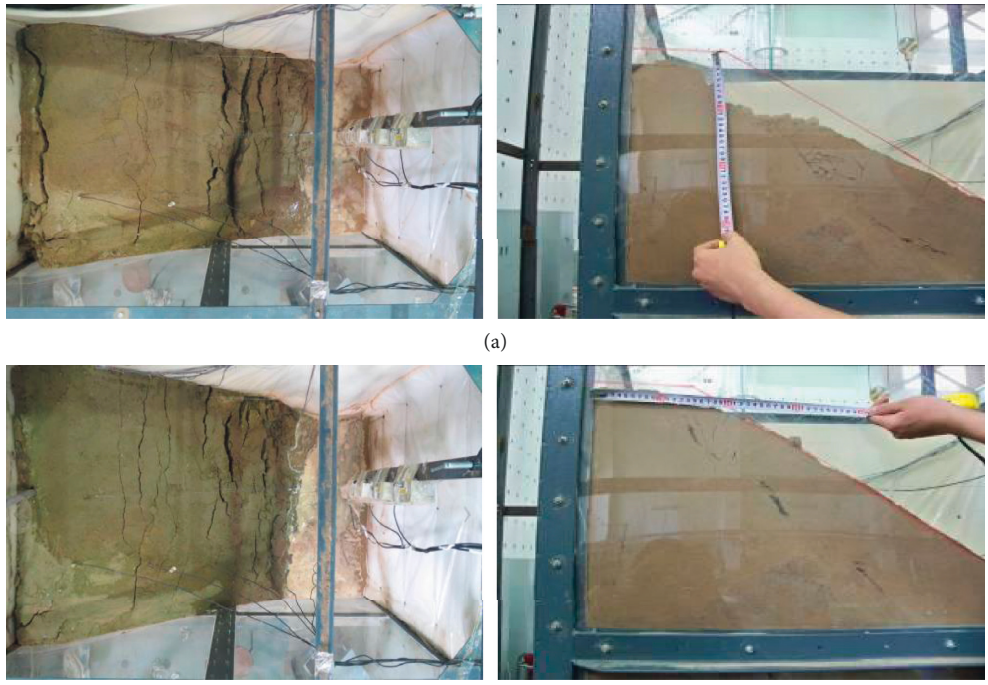

(a)

(b)

Figure 23: Plastic failure of the slope before and after strengthening. (a) Plastic failure of the slope before strengthening. (b) Plastic failure of the slope after strengthening.

5. Conclusions

(1) New cementitious composite materials were developed by using mineral powder, magnesia, quicklime, and gypsum. And the optimal proportion of different components in the new cementitious composite materials was determined through a series of tests and analyses.

(2) New cementitious composite materials were used to solidify saline soils, and the materials not only solidified saline soil to endow the soil with certain strength but also absorbed Cl^- to reduce the harm. The SEM analysis result showed that the saline soil solidified by the new cementitious composite materials had compact internal structure and uniformly distributed soil particles.

(3) New cementitious composite materials were applied to strengthen the saline soil subgrade in a highly seismic region. The results show that the newly developed cementitious composite materials have better aseismic behaviour, and the materials significantly reduced the seismic dynamic response and damage degree of the subgrade. This work provides important technological guidance for seismic design of saline soil subgrades.

Data Availability

The data used to support the findings of this study are available from the corresponding author upon request.

Conflicts of Interest

The authors declare that they have no conflicts of interest.

Acknowledgments

This study was financially supported by a research grant from the Institute of Crustal Dynamics, China Earthquake Administration (no. ZDJ2019-10), National Natural Science Foundation of China (grant no. 51708516), the Young Elite Scientists Sponsorship Program by CAST (2018QNRC001), Beijing Municipal Natural Science Foundation (8174078), National Key R&D Program of China (2017YFC1500404), and Natural Science Foundation of Hebei Province (E23019210126).

References

[1] T. Wen, *Study of Engineering Properties and Improvement of Loessial Sulfate Saline Soil in the Northwest area*, Lanzhou University of Technology, Lanzhou, China, 2012.

[2] X. Yang, Z. You, F. Niu et al., "Research progress in stabilizers and their effects in improving physical and mechanical properties of saline soil," *Journal of Glaciology and Geocryology*, vol. 36, no. 2, pp. 376–385, 2014.

[3] W. Li and S. Chai, "Evaluation of solidifying effect of SH agent on inshore saline soils," *Journal of Engineering Geology*, vol. 26, no. 2, pp. 407–415, 2018.

[4] Y. Wen, W. Zhang, Y. Luo, X. Liu, B. Li, and L. Wang, "Analysis of gradation characteristics and salt-resistance effect of subgrade layer in saline soil area," *Journal of Qinghai University*, vol. 36, no. 4, pp. 17–23, 2018.

[5] B. Song, L. Wang, and D. Zhu, "Subgrade design and construction technology in saline soil area," *Subgrade Engineering*, vol. 2, pp. 160–162, 2011.
[6] S. Zhang, Y. Wang, F. Xiao, and W. Chen, "Effect of overburden load on salt expansion of gravelly sand sulfate saline soil Subgrade," *China Railway Science*, vol. 40, no. 2, pp. 1–8, 2019.
[7] Y. Zhang, T. Zhang, R.-F. Zhang, and W. Yao, "Research on the selection of a railway subgrade filler in high saline soil region," *Journal of Railway Engineering Society*, vol. 33, no. 9, pp. 10–13, 2016.
[8] H. Li, R. Yin, and M. Zhang, "Study on use of gravel improved saline soil as subgrade fill," *Subgrade Engineering*, vol. 172, no. 1, pp. 53–57, 2014.
[9] L. Qingfeng, G. Zhou, S. Wang, Z. Huo, and B. Ma, "Microstructure characteristics of solidified saline soil based on nuclear magnetic resonance," *Rock and Soil Mechanics*, vol. 40, no. 1, pp. 245–249, 2019.
[10] F. Qi and W. Liu, "Subgrade design and construction technology in saline soil area," *Railway Construction Technology*, vol. 8, pp. 69–72, 2015.
[11] S. Zhang, S. Xie, X. Yang, and W. Chen, "Action mechanism of coarse particle sulfate soil subgrade modified by volcanic ash," *Chinese Journal of Geotechnical Engineering*, vol. 41, no. 3, pp. 588–594, 2019.
[12] Y. Cheng, H. Yu, B.-l. Zhu, and D.-X. Wei, "Laboratory investigation of the strength development of alkali-activated slag-stabilized chloride saline soil," *Journal of Zhejiang University-Science A*, vol. 17, no. 5, pp. 389–398, 2016.
[13] GB175-2007, Common portland cement, 2007.
[14] Z. Jin and P. Wang, "A laboratorial study of system"slag-light burnt magnesia-alkali"as cementitious material," *Material Applications*, vol. 33, no. 5, pp. 1–3, 2005.
[15] Z. Lou, Q. Ye, H. Chen, Y. Wang, and J. Shen, "Hydration of mgo in clinker and its expansion property," *Journal of the Chinese Ceramic Society*, vol. 4, pp. 430–436, 1998.
[16] J. Harrison, "New cements based on the addition of reactive magnesia to Portland cement with or without added pozzolan," in *Proceedings of the CIA Conference: Concrete in the Third Millenium*, pp. 24–35, CIA, Brisbane, Australia, 2003.
[17] M. Liska, L. J. Vandeperre, and A. Al-Tabbaa, "Influence of carbonation on the properties of reactive magnesia cement-based pressed masonry units," *Advances in Cement Research*, vol. 20, no. 2, pp. 1–12, 2008.
[18] China Railway Siyuan Survey and Design Group C, *Technical Code on Dry Jet Mixing Method to Stabilized Soft Foundation (TB 10113-96)*, Ministry of Railways, Beijing, China, 1996.
[19] C. Liu, *Study on Mechanism and Performance of the Coastal Saline Soil Cured by Slag Composite Curing agent*, University of Science and Technology Beijing, Beijing, China, 2015.
[20] Ministry of Railways of the People's Republic of China, *Code for Seismic Design of Railway Engineering (GB50112-2009)*, China Planning Press, Beijing, China, 2006.
[21] L. Brand, "The Pi theorem of dimensional analysis," *Archive for Rational Mechanics and Analysis*, vol. 1, no. 1, pp. 35–45, 1957.
[22] L. Jiang, L. Yao, and J. Wang, "Similitude for shaking table model test on side slope relating to dynamic characteristics and strength," *Journal of Transport Science and Engineering*, vol. 25, no. 2, pp. 1–7, 2009.